ATLAS NOTE

ATLAS-CONF-2013-052

May 13, 2013

A search for $t\bar{t}$ resonances in lepton plus jets events with ATLAS using 14 fb^{-1} of proton-proton collisions at $\sqrt{s} = 8$ TeV

The ATLAS Collaboration

Abstract

A search for new particles that decay into top quark pairs ($t\bar{t}$) is performed with the ATLAS experiment at the LHC using an integrated luminosity of 14 fb^{-1} of proton-proton collision data collected at center-of-mass energy $\sqrt{s} = 8$ TeV. The lepton plus jets final state is used, where the top-pair decays as $t\bar{t} \to W^+bW^-\bar{b}$ with one W boson decaying leptonically and the other hadronically. The $t\bar{t}$ system is reconstructed using both a conventional resolved jet analysis and a large-radius jet substructure analysis. The $t\bar{t}$ invariant mass spectrum is searched for local excesses deviating from the Standard Model prediction. No evidence for a $t\bar{t}$ resonance is found and 95% CL limits on the production rate are determined for massive states in two benchmark models. The upper limits on the cross section times branching ratio of a narrow Z' boson decaying to top pairs range from 5.3 pb for a resonance mass of 0.5 TeV to 0.08 pb for a mass of 3 TeV. A narrow leptophobic topcolor Z' boson with a mass below 1.8 TeV is excluded. Upper limits are set on the cross section times branching ratio for a broad color-octet resonance with $\Gamma/m = 15.3\%$ decaying to $t\bar{t}$. These range from 9.6 pb for a mass of 0.5 TeV to 0.152 pb for a mass of 2.5 TeV. A Kaluza-Klein excitation of the gluon in a Randall–Sundrum model is excluded for masses below 2.0 TeV.

1 Introduction

One of the primary goals of experiments at the LHC is the search for new physics beyond the Standard Model (SM). Many theories of new physics predict the existence of new particles, and some predict new heavy bosons that decay primarily into $t\bar{t}$ pairs. Examples of these theories include topcolor models [1], chiral color models [2] and Randall–Sundrum models with warped extra dimensions [3–7].

The ATLAS experiment searches for the production of top quark pair ($t\bar{t}$) resonances produced in proton-proton (pp) collisions at a center-of-mass energy of 8 TeV using a data set collected in 2012 with an integrated luminosity of $14.3\,\mathrm{fb}^{-1}$. The search is carried out in the lepton plus jets decay channel where one W boson from a top quark decays leptonically (to an electron or a muon, and a neutrino) and the other decays hadronically. The $t\bar{t}$ invariant mass spectrum is tested for any local excess of events that may result from a resonance decaying to $t\bar{t}$. It is reconstructed using a combination of *resolved* and *boosted* reconstruction methods. Using the former, the hadronically decaying top quark is identified by two or three distinct small-radius jets. Using the latter the hadronically decaying top quark is identified by one large-radius jet that has substructure consistent with being composed of the decay products of a W boson and a b quark. High momentum top quark decays are reconstructed more efficiently using the boosted reconstruction technique. For both reconstruction methods, the semileptonically decaying top quark is identified by a lepton, one small-radius jet and missing transverse momentum.

Experiments at the LHC have used two specific theoretical models as benchmarks. The models test the production of resonances with both narrow and broad widths relative to the detector resolution which is of order 7%. The narrow resonance benchmark is a topcolor, leptophobic Z' given by model IV of Harris et al. [8]. Identical model parameters were used by the DØ and the CDF collaborations including a resonance width of $\Gamma_{Z'}/m_{Z'} = 1.2\%$ [9, 10]. The cross section is calculated at leading order (LO) in QCD using CTEQ6L1 [11] parton distribution functions (PDFs) multiplied by a LO to next-to-leading-order (NLO) K-factor of 1.3 as applied in recent ATLAS and CMS searches [12–18] to correct the total inclusive cross section. The K-factor is taken from Ref. [19], but is also consistent with more recent calculations [20].

The broad resonance benchmarks are Kaluza-Klein (KK) gluons that arise in Randall-Sundrum models with an extra dimension with a warped geometry and where all the SM fields and matter can propagate in all five dimensions. The specific model tested is detailed in a previous ATLAS study [21] and is implemented using the MADGRAPH event generator [22]. A resonance width of $\Gamma_{g_{KK}}/m_{g_{KK}} = 15.3\%$ is used. No K-factor from leading order to next-to-leading order is applied for this model since no estimate is available.

Searches for $t\bar{t}$ resonances have been performed by CDF [23] and DØ [24] at the Tevatron, and by ATLAS and CMS at the LHC. The searches at the LHC are carried out in the lepton plus jets, dilepton, and all-hadronic final states, though data using the lepton plus jets final states provide the best sensitivity to the benchmark models. The best CMS limits at 95% credibility level (CL) on the benchmark resonances come from a search using data taken at $\sqrt{s} = 8\,\mathrm{TeV}$ with integrated luminosity of $20\,\mathrm{fb}^{-1}$ [18]. They exclude a leptophobic topcolor Z' with mass smaller than 2.1 TeV and a KK gluon with mass lower than 2.5 TeV. The expected lower mass limits for this CMS search are 2.0 TeV for the leptophobic topcolor Z' and 2.2 TeV for the KK gluon. The best corresponding limits at 95% CL from ATLAS, using data taken at $\sqrt{s} = 7\,\mathrm{TeV}$, exclude a Z' mass lower than 1.7 TeV and a KK gluon with mass smaller than 1.9 TeV [17].

The present analysis is the first $t\bar{t}$ resonance search with ATLAS to use data taken at a center-of-mass energy of 8 TeV. The analysis includes the use of *trimming* [25], which removes soft small-radius subjets within a larger radius jet, to reduce pile-up effects, and an improved algorithm for reconstructing the $t\bar{t}$ system in the boosted selection relative to the one described in Ref. [13].

2 The ATLAS detector

The ATLAS detector [26] is used to identify particles produced in proton-proton collisions at the LHC and measure their momenta. It has a cylindrical geometry and close to 4π solid-angle coverage. The inner detector (ID) covers a pseudorapidity[1] range of $|\eta| < 2.5$ and consists of multiple layers of silicon pixel and strip detectors and a straw-tube transition radiation tracker. The ID is surrounded by a superconducting solenoid that provides a 2 T magnetic field. The calorimeter system surrounds the ID and solenoid and covers the pseudorapidity range $|\eta| < 4.9$. It consists of high-granularity lead and liquid-argon (LAr) electromagnetic (EM) calorimeters, a steel and scintillating-tile hadronic calorimeter within $|\eta| < 1.7$ and two copper and LAr hadronic endcap calorimeters covering $1.5 < |\eta| < 3.2$. Forward copper/LAr and tungsten/LAr calorimeter modules complete the solid-angle coverage out to $|\eta| = 4.9$. The muon spectrometer (MS) resides outside the calorimeters. It consists of multiple layers of trigger and tracking chambers within an air-core toroidal magnetic field, which enables an independent, precise measurement of muon track momenta for $|\eta| < 2.7$. The muon trigger covers $|\eta| < 2.4$.

3 Data and Monte Carlo samples

The data used in this search were collected by the ATLAS detector at the LHC in 2012. The data are only used if they were recorded under stable beam conditions and with all relevant subdetector systems operational. The data sample was collected using a logical OR of two single-muon triggers with transverse momentum thresholds of 24 GeV and 36 GeV and a logical OR of two single-electron triggers with transverse momentum thresholds of 24 GeVand 60 GeV. For both electrons and muons, the triggers with the lower threshold also have an isolation requirement. The integrated luminosities for the electron and muon data sets are $14.3 \pm 0.5\,\mathrm{fb}^{-1}$ and $14.2 \pm 0.5\,\mathrm{fb}^{-1}$ [27, 28], respectively. The mean number of pp interactions per bunch-crossing for these data sets is approximately 20.

Samples of Monte Carlo simulated events are used to predict the contributions from various SM processes to the expected background and to model possible $t\bar{t}$ resonance signals. After event generation, all samples are passed through a GEANT4-based [29] simulation [30] of the ATLAS detector and reconstructed using the same reconstruction software used for data. These simulations include a realistic modelling of the pile-up conditions observed in the data.

The primary irreducible background is SM $t\bar{t}$ production, characterized by a smoothly falling invariant mass spectrum. It is modeled using the MC@NLO v4.01 [31–33] generator, Herwig v6.520 [34] for parton showering and hadronization and Jimmy v4.31 [35] for modeling the multiple parton scattering. The CT10 [36] PDFs are used and the top quark mass is set to 172.5 GeV. Only events in which at least one of the W bosons decays leptonically (including to τ) are modeled. This corresponds to an effective cross section times branching ratio at approximate NNLO (next-to-next-to-leading order) of 129 pb [37, 38], obtained using the calculation described in Section 8.

Single top quark production is modeled using multiple generators. Production in the s-channel and production with an associated W (Wt) are modeled via MC@NLO/Herwig/Jimmy [39,40] with the CT10 PDFs as above. Production in the t-channel is modeled using the AcerMC v3.8 [41] generator and Pythia v6.426 [42] for parton showering and hadronization; the CTEQ6L1 PDF set is used. For the s- and t-channels, events are generated in which the W boson is required to decay leptonically while for the Wt process there is no such requirement. The cross section times branching ratios used are based on approximate NNLO calculations: 28.4 pb (t-channel) [43], 22.4 pb (Wt process) [44] and 1.8 pb

[1] ATLAS uses a right-handed coordinate system with its origin at the nominal interaction point (IP) in the center of the detector and the z-axis along the beam pipe. The x-axis points from the IP to the center of the LHC ring, and the y-axis points upward. Cylindrical coordinates (r, ϕ) are used in the transverse plane, ϕ being the azimuthal angle around the beam pipe. The pseudorapidity is defined in terms of the polar angle θ as $\eta = -\ln\tan(\theta/2)$.

(s-channel) [45].

Leptonic decays of W and Z bosons, including those to τ, accompanied by jets are an important background. The samples are generated with Alpgen v2.13 [46] with up to five extra final state partons at leading order without virtual corrections. Modeling of parton showering, hadronization and underlying events uses Pythia v6.426 and the matching of the matrix element to the parton shower is done using the MLM method [47]. The PDF set used is CTEQ6L1. Specific W boson plus heavy flavor processes ($Wb\bar{b}$, $Wc\bar{c}$ and Wc) are generated separately with Alpgen and double counting of the heavy flavor contributions is removed from the W plus light quark jets samples. The W+jets samples are normalized to the inclusive NNLO cross sections [48, 49] and then corrected using data as described in Section 7. The Z+jets samples include contributions from the interference between photon and Z boson exchanges and events are required to have a dilepton invariant mass $40 < m_{\ell\ell} < 2000$ GeV. The $Zb\bar{b}$ and $Zc\bar{c}$ processes are generated separately with Alpgen and overlap removal is done as in the W+jets case.

The massive-diboson background is modeled using Herwig v6.520 and Jimmy v4.31 with CTEQ6L1 PDFs. A filter requiring the presence of at least one lepton with $p_{\mathrm{T}} > 10$ GeV and $|\eta| < 2.8$ is used. The NLO (next-to-leading order) cross sections used for the samples before filtering are 20.9 pb for WW production, 7.0 pb for WZ production, and 1.5 pb for ZZ production [50].

Signal samples of topcolor Z' are modeled using the Sequential Standard Model [51] $Z' \to t\bar{t}$ process as implemented in Pythia v8.165 [52] with MSTW2008LO [53] PDFs. The width of the generated Z' is $\sim$3% of the mass, which is negligible compared to the detector resolution. A K-factor of 1.3 [19] is applied to account for NLO effects.[2] Signal samples of Randall–Sundrum KK gluons were generated via Madgraph [22] and then hadronized using Pythia v8.165. The width of the KK gluon is 15.3% of its mass and its branching fraction to $t\bar{t}$ is 92.5% [3].

4 Object selection

Jets are reconstructed using the anti-k_t algorithm [54] applied to topological clusters [55] of calorimeter cells. Jets with radius parameters of $R = 0.4$ and $R = 1.0$ are used. The topological clusters used as input to the algorithm are locally calibrated [56–58] to compensate for differing calorimeter response to hadronic and electromagnetic showers. Large-radius jets have jet trimming [25] applied. In trimming, subjets are formed by applying a (possibly different) jet algorithm with smaller radius parameter, R_{sub}, and then soft subjets with less than a certain fraction, f_{cut}, of the original jet p_T are removed. The properties of the trimmed jet are then calculated using the surviving subjets. This procedure mitigates the effect of pileup [59]. The trimming parameters used in this search are $f_{\mathrm{cut}} = 0.05$ and $R_{\mathrm{sub}} = 0.3$, the inclusive k_t [60] algorithm is used to form the subjets as proposed in Ref. [25]. Both small-radius and large-radius jets have their final transverse momentum and pseudorapidity corrected with energy and η dependent correction factors derived from simulation [58, 61]. The uncertainties of such corrections are derived from data [58, 62]. An additional selection criterion for small-radius jets is that the jet vertex fraction (JVF) exceeds 0.5. The JVF parameter is defined as the summed transverse-momentum, p_{T}, of all tracks matched to the jet from the primary vertex[3] divided by the summed p_{T} of all matched tracks from all vertices. The small-radius jets are selected with $p_{\mathrm{T}} > 25$ GeV and $|\eta| < 2.5$, while large-radius jets must have $p_{\mathrm{T}} > 300$ GeV and $|\eta| < 2.0$.

The tagging of small-radius jets associated with the decay of b-quarks is used in both the resolved and boosted reconstructions. A neural-network-based b-tagging algorithm, MV1, that uses the output weights of impact parameter, secondary vertex, and decay topology algorithms is employed [63]. The

[2] A recent full NLO calculation [20] gives smaller K-factors. This difference is attributable to the kinematic cuts applied, radiative corrections for top-quark decays and usage of different PDF sets. However, when using the same set-up as in Ref. [19] a consistent K-factor is obtained. The setup used for signal generation in this paper corresponds more closely to Ref. [19].

[3] The primary vertex in the event is the vertex with highest summed p_T^2 for associated tracks.

operating point chosen corresponds to an average b-tagging efficiency in simulated $t\bar{t}$ events of 70% and a light quark rejection factor of 140 for $p_{\mathrm{T}} > 20$ GeV. No b-tagging information for large-radius jets is used.

Electrons are identified by the shape of the shower in the electromagnetic calorimeter and the characteristics of the matching track in the ID [64]. The cluster in the EM calorimeter is required to lie in the range $|\eta| < 2.47$ and the calorimeter transition region $1.37 < |\eta| < 1.52$ is excluded. The electron transverse energy, E_{T}, is reconstructed using the cluster energy and track pseudorapidity and must be greater than 25 GeV, to ensure a fully efficient trigger. Electrons are defined to be isolated if their *mini-isolation* [17, 65], I_{mini}, satisfies $I_{\mathrm{mini}} < 0.05 E_{\mathrm{T}}$. The variable I_{mini} is defined as the sum of the p_{T} of tracks not associated with the lepton within an $\eta - \phi$ cone of size 10 GeV$/E_{\mathrm{T}}$. The reduction in the size of the cone with increasing lepton transverse momentum is well suited for semileptonic decays of high p_{T} top quarks, where the lepton and b-jet tend to be closer together at higher top-quark p_{T}. The performance of the mini-isolation selection is very stable for different $t\bar{t}$ kinematic regimes, as shown in Appendix A. Finally, the z-impact parameter relative to the primary vertex should be less than 2 mm.

Muons are identified using matched tracks in the MS and in the ID. The muon momentum is calculated using both the MS and ID tracks and corrected for energy loss in the calorimeter. The transverse momentum, p_{T}, of the muon must be greater than 25 GeV. Muons are required to lie in the range $|\eta| < 2.5$. The same mini-isolation criteria used for electrons is also applied to muons, namely $I_{\mathrm{mini}}/p_{\mathrm{T}} < 0.05$. Similarly, the z-impact parameter relative to the primary vertex should be less than 2 mm.

Overlapping physics objects are subject to the following removal procedure. Firstly, Muons with $\Delta R(\mu, j) = \sqrt{\Delta\eta^2 + \Delta\phi^2} < 0.1$ between the muon and nearest small-radius jet are removed since their likely origin is non-prompt lepton production. Secondly, electrons with $\Delta R(e, j) < 0.4$ to any remaining small-radius jet are removed because of the difficulty in electron identification. Subsequent event selection cuts, described in Section 5, ensure that there is no overlap between the large-R jets used in the analysis and leptons.

The missing transverse momentum, $E_{\mathrm{T}}^{\mathrm{miss}}$, is calculated from the vector sum of the transverse energy in calorimeter cells associated with topological clusters [66]. Calorimeter cells are first uniquely associated with a physics object (e.g., electron, jet or muon) and the transverse energy of each cell is then calibrated according to the object to which it belongs. The reconstructed muon transverse momentum is used along with the cells of isolated and non-isolated muons. Cells associated with any low-p_{T} jets ($10 < p_{\mathrm{T}} < 20$ GeV) and cells not associated any high-p_{T} object are also included in the vector sum.

5 Event selection

The event selection is designed to have a high efficiency for events with high p_{T} top quarks, while minimizing non $t\bar{t}$ backgrounds. Events are required to pass a high-p_{T} single-electron or single-muon trigger and must have exactly one associated reconstructed electron or muon candidate. Events must have a reconstructed primary vertex with at least five tracks with $p_{\mathrm{T}} > 0.4$ GeV. In the $e+$ jets channel, $E_{\mathrm{T}}^{\mathrm{miss}}$ must be larger than 30 GeV and the transverse mass larger than 30 GeV. The transverse mass is defined as $m_{\mathrm{T}} = \sqrt{2 p_{\mathrm{T}} E_{\mathrm{T}}^{\mathrm{miss}} (1 - \cos\Delta\phi)}$, where p_{T} is the transverse momentum of the charged lepton and $\Delta\phi$ is the azimuthal angle between the charged lepton and the missing transverse momentum. In the $\mu+$ jets channel, the selection is $E_{\mathrm{T}}^{\mathrm{miss}} > 20$ GeV and $E_{\mathrm{T}}^{\mathrm{miss}} + m_{\mathrm{T}} > 60$ GeV. These selection criteria are used to suppress multi-jet backgrounds.

Events can be placed in either the boosted or resolved reconstruction samples. The boosted sample consists of events with at least one small-radius jet and at least one large-radius jet. The *selected* small-radius jet, j_{sel}, is the highest-p_{T} jet satisfying $\Delta R(\ell, j) < 1.5$ where ℓ is the selected lepton. In addition to satisfying the kinematic requirements described previously, the large radius-jet must have jet mass

$m_{\text{jet}} > 100\,\text{GeV}$. An additional jet substructure requirement is made; the large-radius jet is reclustered with the exclusive k_t jet algorithm [60] and the first k_t splitting scale, $\sqrt{d_{12}}$, must satisfy $\sqrt{d_{12}} > 40\,\text{GeV}$. This splitting scale is expected to have higher values for jets that have two hard subjets, such as jets that fully enclose the decay products of hadronically decaying top quarks, than for other jets. Furthermore the large radius jet must be well separated from the lepton and selected small-radius jet: $\Delta R(\text{jet}, j_{\text{sel}}) > 1.5$ and $\Delta\phi(\text{jet}, \ell) > 2.3$. Finally, there must be at least one small-radius jet which is b-tagged.

Events that fail the boosted selection are subsequently examined using the resolved selection criteria. In the resolved selection, the event must have at least four small-radius jets satisfying $p_{\text{T}} > 25\,\text{GeV}$, $|\eta| < 2.5$ and with jet-vertex-fraction larger than 0.5. Alternatively events with only three small-radius jets are accepted if one of those jets has mass greater than 60 GeV. As in the boosted selection, there must be at least one small-radius jet that is b-tagged.

Two typical events selected by the boosted selection are displayed in Appendix C. These events also fulfill the requirement of the resolved selection.

Thus events are placed into one of four disjoint categories corresponding to the e+jets (where one W decays to electron and neutrino) and μ+jets (where one W decays to muon and neutrino) decay channels and either boosted or resolved reconstruction selection criteria. The efficiency[4] of the selection on simulated $Z' \to t\bar{t}$ events is shown as a function of the invariant mass, at parton level[5], of the top and antitop pair ($m_{t\bar{t}}$) in Figure 1. The boosted selection becomes important above 1 TeV. Further efficiencies for different subselections are shown in Appendix B.

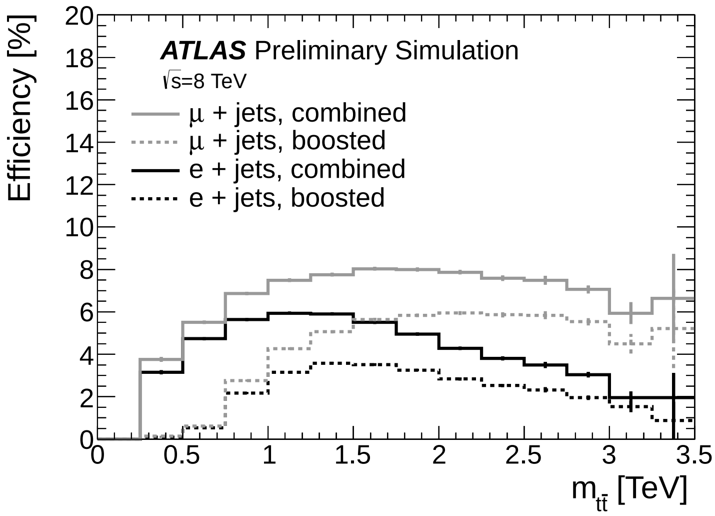

Figure 1: The selection efficiency as a function of the true $m_{t\bar{t}}$ for $Z' \to t\bar{t}$ events. The μ+jets channel is shown with gray lines and the e+jets channel with black lines. Dashed lines show the boosted selection and solid lines the total selection efficiency. The error bars indicate statistical uncertainties.

6 Event reconstruction

The $t\bar{t}$ candidate invariant mass, $m_{t\bar{t}}^{\text{reco}}$, is computed from the four-momenta of the physics objects in the event. For the semileptonically decaying top quark, in both the resolved and the boosted selections,

[4]This efficiency includes both geometrical acceptance and the object selection efficiency within the fiducial region.

[5]In this case the *parton level* top quarks are those in the PYTHIA event record immediately before they decay.

the longitudinal component of the neutrino momentum, p_z, is computed by imposing an on-shell W boson mass constraint on the lepton plus $E_{\mathrm{T}}^{\mathrm{miss}}$ system. If two real solutions exist, then the solution with the smallest $|p_z|$ is chosen in the boosted selection while both are tested for the resolved selection. In events where no real solution is found, the $E_{\mathrm{T}}^{\mathrm{miss}}$ is rescaled and rotated, applying the minimum variation necessary to find exactly one real solution [67]. This procedure is justified since mismeasurement of the missing transverse energy is the most likely explanation for a lack of solution to the p_z equation, assuming that the lepton indeed comes from a W boson decay.

For the resolved reconstruction, a χ^2 algorithm is used to select the best assignment of jets to the hadronically and semileptonically decaying top quarks. The χ^2 algorithm uses the reconstructed top quark and W boson masses as constraints. All possible permutations for four or more jets are tried and the permutation with the lowest χ^2 is used to calculate $m_{t\bar{t}}^{\mathrm{reco}}$. If there are two solutions for the neutrino longitudinal momentum, both are tried as well. The χ^2 algorithm is:

$$\begin{aligned}\chi^2 &= \left[\frac{m_{jj}-m_W}{\sigma_W}\right]^2 \\ &+ \left[\frac{m_{jjb}-m_{jj}-m_{t_h-W}}{\sigma_{t_h-W}}\right]^2 + \left[\frac{m_{j\ell\nu}-m_{t_\ell}}{\sigma_{t_\ell}}\right]^2 \\ &+ \left[\frac{(p_{\mathrm{T},jjb}-p_{\mathrm{T},j\ell\nu})-(p_{\mathrm{T},t_h}-p_{\mathrm{T},t_\ell})}{\sigma_{\mathrm{diff}p_{\mathrm{T}}}}\right]^2, \end{aligned} \tag{1}$$

where the expected mean mass (m), transverse momentum (p_{T}) and the standard deviations (σ) in each term are derived from Monte Carlo simulation.[6] The hadronically and semi-leptonically decaying top quarks are denoted by t_h and t_ℓ, respectively, and j and b denote the jets originating, respectively, from the light quarks and b quarks. The first term is the mass constraint for the hadronically decaying W boson. The second term corresponds to the invariant mass of the hadronically decaying top quark, but since the invariant mass of the jets from the W candidate (m_{jj}) is heavily correlated with the mass of the three jets from the hadronic top candidate (m_{jjb}), the mass of the hadronically decaying W boson is subtracted to decouple this term from the first one. The third term represents a mass constraint on the semi-leptonically decaying top quark, and the last term weakly constrains the transverse momenta of the two top quarks to be similar, as expected for a resonance decay or SM $t\bar{t}$ production. The parameters are determined from Monte Carlo simulation studies comparing partons from the top quark decay with reconstructed objects.

If one of the jets has a mass larger than 60 GeV, the χ^2 is slightly modified:

$$\chi^2 = \left[\frac{m_{jJ}-m_{jJ}^{t_h}}{\sigma_{jJ}^{t_h}}\right]^2 + \left[\frac{m_{j\ell\nu}-m_{t_\ell}}{\sigma_{t_\ell}}\right]^2 + \left[\frac{(p_{\mathrm{T},jJ}-p_{\mathrm{T},j\ell\nu})-(p_{\mathrm{T},t_h}-p_{\mathrm{T},t_\ell})}{\sigma_{\mathrm{diff}p_{\mathrm{T}}}}\right]^2, \tag{2}$$

with J referring to the high-mass jet, and where the dijet mass-difference term, $m_{jJ} - m_{jJ}^{t_h}$, allows the merging of either both quarks from W boson decay, or one quark from W boson decay with the b quark from top quark decay.[7]

For the boosted reconstruction, there is no ambiguity in the assignment of jets. The hadronically decaying top quark four-momentum is taken to be that of the large-radius jet, while the semi-leptonically decaying top quark four-momentum is formed from the neutrino solution from the W boson mass constraint, the high-p_{T} lepton and the selected small-radius jet.

[6]The values used are m_W = 83.3 GeV, m_{t_h-W} = 91.1 GeV, m_{t_ℓ} = 168.2 GeV, σ_W = 10.8 GeV, σ_{t_h-W} = 14.2 GeV, σ_{t_ℓ} = 20.6 GeV, $p_{\mathrm{T},t_h} - p_{\mathrm{T},t_\ell} = -8.7$ GeV and $\sigma_{\mathrm{diff}p_{\mathrm{T}}}$ = 55.0 GeV.

[7]The values of $m_{jJ}^{t_h}$ and $\sigma_{jJ}^{t_h}$ are determined from simulation to be 173.5 GeV and 16.3 GeV, respectively.

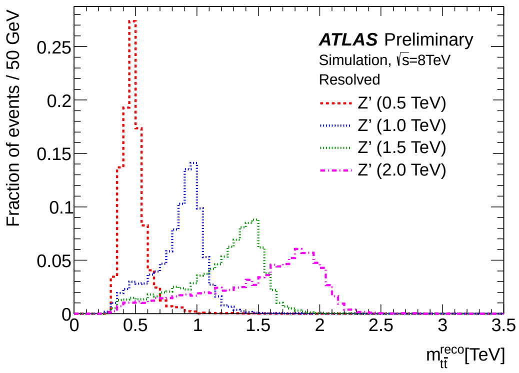

(a) Reconstructed $t\bar{t}$ mass in the resolved selection.

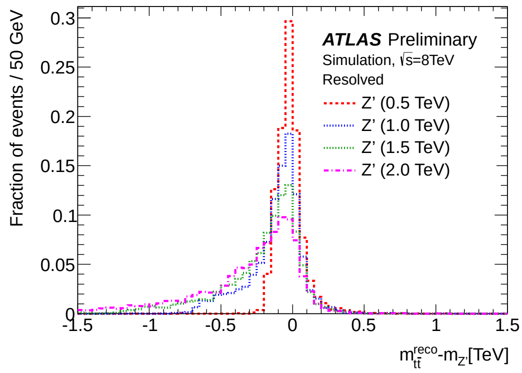

(b) Residuals for the $t\bar{t}$ mass in the resolved selection.

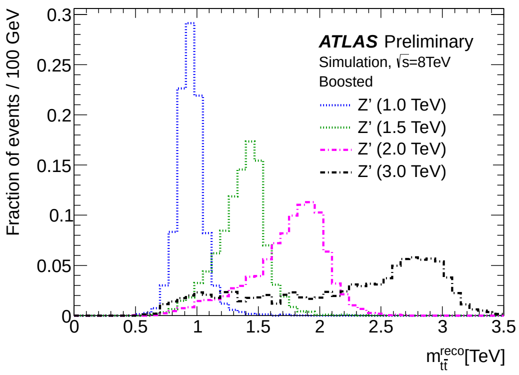

(c) Reconstructed $t\bar{t}$ mass in the boosted selection.

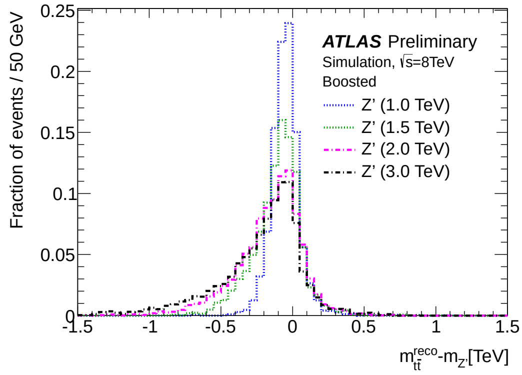

(d) Residuals for the $t\bar{t}$ mass in the boosted selection.

Figure 2: The reconstructed $t\bar{t}$ invariant mass, $m_{t\bar{t}}^{\mathrm{reco}}$, and the corresponding difference between true and reconstructed invariant mass using the resolved (a,b) and boosted selection (c,d), for a range of narrow Z' masses.

Figure 2 shows the reconstructed boson masses for four hypothesized Z' masses together with the corresponding difference between true and reconstructed mass. The tails of the high-mass resonances in the distributions of Figure 2 are mainly caused by the convolution of the Z' line shape and the steeply falling parton distribution functions.

7 Backgrounds determined from data

Two important backgrounds, W+jets and multi-jet production, are estimated partially or fully from data.

The W+jets background for events passing the resolved selection, including its shape, is estimated based on samples of simulated ALPGEN events. The fractions of different flavor components ($W + b\bar{b}$, $c\bar{c}$, c and light quarks) are rescaled by a set of factors extracted from a W+jets dominated region, where the b-tagging requirement is removed and the existence of exactly two jets is required. These scale factors are determined separately for each channel by comparing the data and expected background in subsamples of different b-jet and lepton charge. They are then extrapolated into higher-jet-multiplicity bins with the assumption of constant relative ratio while keeping the overall normalization unchanged.

The overall yields of W+jets events are then normalized by comparing the observed charge-asymmetry of W boson production from data [68, 69] and the predicted charge-asymmetry from Monte Carlo:

$$N_{W^+} + N_{W^-} = \left(\frac{r_{\mathrm{MC}} + 1}{r_{\mathrm{MC}} - 1}\right)(D_{\mathrm{corr}+} - D_{\mathrm{corr}-}), \tag{3}$$

where r_{MC} is the ratio between the W^+ to W^- boson event yields in Monte Carlo after selection, and $D_{\mathrm{corr}+(-)}$ is the number of observed events with a positively (negatively) charged lepton. Charge-symmetric contributions from $t\bar{t}$, Z+jets and multi-jet processes cancel in the difference. Slightly charge asymmetric contributions from the remaining backgrounds such as single top are estimated using Monte Carlo simulation. This is again performed without any b-tagging requirement and for different lepton flavors and jet multiplicity bins respectively. The resulting normalization scale factors are consistent with unity within statistical and systematic uncertainties of approximately 17%.

A similar but modified method is used to determine the W+jets normalization for the events passing the boosted selection. In this case, the same formula is used as above, a W+jets dominated sample is obtained by applying the boosted selection but without the b-tagging, $\Delta\phi(\mathrm{jet}, l) > 2.3$, jet mass and $\sqrt{d_{12}}$ requirements. The resulting scale factor for the W+jets normalization is approximately 0.65 (0.80) for the electron (muon) channel but with a combined statistical and systematic uncertainty of approximately 19%. The systematic uncertainties considered for the W+jets estimation, in both the resolved and boosted selections, include flavor-fraction uncertainties and MC uncertainties as well as other resolution, reconstruction and identification efficiency uncertainties.

The normalization and shape of the multi-jet background are determined directly from data using a *matrix method* [70] for both resolved and boosted selections. This method makes use of samples of events that possess similar kinematic characteristics but are enriched in multi-jet events, obtained with relaxed lepton identification criteria such as isolation requirement. The yields and kinematic distributions of multi-jet background in the signal region can then be derived by applying the efficiency and false-identification rate of the relaxed selection on such sample. The efficiency is estimated from Monte Carlo samples of prompt lepton sources, and validated against data. The false-identification rate is directly estimated from data in a multi-jet-enriched control region by requiring low $E_{\mathrm{T}}^{\mathrm{miss}}$ and m_{T}, as well as a high transverse impact parameter significance. For the boosted channel, this control region is further purified by requiring the absence of a high-mass large-radius jet with $p_{\mathrm{T}} > 150$ GeV.

A conservative 50% systematic uncertainty is assigned to the predicted multi-jet yields, motivated by considering changes in the estimation from alternative loose lepton definition, parameterization of the efficiency and the false-identification rate, and control region selection. The modelling of the $m_{t\bar{t}}^{\mathrm{reco}}$ shape is also tested in the multi-jet-enriched control region with satisfactory results.

8 Systematic uncertainties

The final discriminating observables are the four $t\bar{t}$ invariant mass spectra (two selections and two decay channels). The uncertainties can be broadly divided into two categories: uncertainties that affect reconstructed objects (such as jets) and uncertainties that affect the modeling of certain backgrounds or signals. Some of the uncertainties affect both the shape and the normalization of the spectrum, while others affect the normalization only.

The dominant normalization uncertainty on the total background is the $t\bar{t}$ cross section uncertainty of 11%. The uncertainty has been calculated at approximate NNLO in QCD [37] with Hathor 1.2 [38] using the MSTW2008 90% CL NNLO PDF sets [53] together with α_S uncertainties [71]. Furthermore, variations from changing the top quark mass by ± 1.25 GeV are added in quadrature to this normalization uncertainty (shape effects are also considered as described below). These uncertainties are then added in quadrature to the normalization and factorization scale uncertainty and found to give consistent results with the NLO+next-to-next-to-leading-logarithm (NNLL) calculation of Ref. [72] as implemented in Top++ 1.0 [73].

The W+jets normalization is varied within the uncertainty on the data-driven determination, corresponding to 18% and 16% for the resolved selection in the electron and muon channels, respectively; and 22% and 16% for the boosted selection in the electron and muon channels, respectively. Three variations of the flavor composition are considered, including the statistical uncertainty on their data-driven determination, the uncertainty on the extrapolation to different jet multiplicities and the correlations between different flavor fractions. These three variations are: increasing the $W + b\bar{b}, c\bar{c}, c$ relative to W+light jets sample, increasing the $W + b\bar{b}$ fraction and increasing the $W + c$ fraction. The normalization uncertainty on the multi-jet background is 50%, as described in Section 7.

The single top background normalization uncertainty [43–45] is 7.7%. The normalization uncertainty on the Z+jets sample is 48%, estimated using Berends-Giele-scaling [50]. The diboson normalization uncertainty is 34%, which is a combination of the NLO PDF and scale uncertainties and additional uncertainties from each selected jet.

The luminosity uncertainty is 3.6% [27, 74] and is applied to the signal samples and all backgrounds except multi-jet and W+jets, which are estimated from data.

Electroweak virtual corrections (Sudakov corrections) for the true $t\bar{t}$ mass dependent scale factors are estimated as given by Manohar et al. [75]. The corrections are modelled using a parametrization of the corrections as a function of $m_{t\bar{t}}$ and grow in size from about 3% at a 0.5 TeV to about 9% at 2 TeV. The shifted spectra are used as the one standard deviation benchmark point of this effect. Since these corrections are only the virtual corrections and it is assumed that the total correction (including the real part) is smaller, they are not used as a correction to the central value, but as an upper limit on the possible size of the (absolute value of the) correction, and hence treated as a systematic uncertainty.

The PDF uncertainty on all MC samples is estimated by taking the envelope of the MSTW2008NLO, NNPDF2.3 [76] and CT10 PDF set uncertainties at 68% CL [8] following the PDF4LHC recommendation [77] and normalizing to the nominal cross section. The PDF uncertainty on the $t\bar{t}$ mass spectrum has a much larger effect on the boosted sample than the resolved sample. The effect on the total background yield is 1.6% (6%) after the resolved (boosted) selection. The size of the uncertainty grows with reconstructed mass attaining values of 15–20% (20–40%) above 2 TeV in the resolved (boosted) selection. The relatively small uncertainty on the resolved selection at high $m_{t\bar{t}}^{\mathrm{reco}}$ arises because there is a larger

[8] The CT10 PDF uncertainties are scaled down by a factor 1.645 to reach an approximate 68% CL.

contribution from events that migrate upwards from low $m_{t\bar{t}}$, where the PDF uncertainty is smaller, than in the boosted selection.

One of the dominant uncertainties affecting reconstructed objects is the jet energy scale (JES) uncertainty, especially for large-radius jets [61, 78], which has an impact of 17% on the overall background yield in the boosted selection. This uncertainty also includes variations in the jet mass scale (JMS) and the k_t splitting scales within their uncertainties [61]. Due to the steeply falling SM jet p_T distribution, the size of this systematic uncertainty on the background tends to fall with increasing $m_{t\bar{t}}^{\mathrm{reco}}$: varying from 25% at lowest masses to about 10% from 1.5 TeV. The impact is smaller for the resolved selection, since the large-radius jets are only used indirectly there, in the veto of events that pass the boosted selection. For small-radius jets, the uncertainties in the JES, the jet reconstruction efficiency and the jet energy resolution (JER) are considered [58]. The small-radius JES is one of the most significant systematics in the resolved-selection, changing the overall expected yield by 6%. The b-tagging uncertainty is modeled through simultaneous variations of the uncertainties on the efficiency and rejection scale factors [63, 79]. An additional b-tagging uncertainty[9] is applied for high-momentum jets ($p_{\mathrm{T}} > 200$ GeV) to account for uncertainties in the modeling of the track reconstruction in high p_{T} environments. The effect of uncertainties associated with the jet vertex fraction is also considered.

The uncertainty on the $t\bar{t}$ background due to uncertainties in the modeling of QCD initial- and final-state radiation (ISR/FSR) is estimated using AcerMC [41] v3.8 plus Pythia v6.426 Monte Carlo samples by varying the Pythia ISR and FSR parameters while retaining consistency with a previous ATLAS measurement of $t\bar{t}$ production with a veto on additional central jet activity [80]. The QED ISR/FSR uncertainty is negligible at this level. The dependency on the $m_{t\bar{t}}^{\mathrm{reco}}$ shape from the choice of NLO generator is accounted for by using the difference between samples generated with MC@NLO and Powheg+Herwig as a systematic uncertainty. The parton showering and fragmentation uncertainty on the $t\bar{t}$ background is estimated by comparing the result from a sample generated with Powheg [81], interfaced with Pythia or Herwig. The uncertainty on the shape of the $m_{t\bar{t}}^{\mathrm{reco}}$ distribution from the value of the top quark mass is evaluated by comparing the shapes of samples generated with top masses of 170 and 175 GeV using MC@NLO and dividing the difference by 4 (to approximate a 1.25 GeV uncertainty).

For the W+jets background, the uncertainty on the shape of the mass distribution is estimated by varying the parameterization of the renormalization and factorization scale [46] and by varying the minimum p_{T} of extra partons generated in the matrix element.

For the leptons, the uncertainties in the mini-isolation efficiency, the single lepton trigger and the reconstruction efficiency are estimated using $Z \to ee$ and $Z \to \mu\mu$ events. In addition, high-jet-multiplicity $Z \to \ell\ell$ events are studied, from which extra uncertainties on the mini-isolation efficiency are assigned to account for the difference between Z and $t\bar{t}$ events. Uncertainties in the $E_{\mathrm{T}}^{\mathrm{miss}}$ reconstruction, as well as for the energy scale and resolution of the leptons are also considered, and generally have a smaller impact on the yield and the expected limits than the uncertainties mentioned above.

In Table 1, an overview of the effects of the dominant systematic uncertainties on the background and signal yields is given. Only the impact on the overall normalization is shown in the table, but some of the systematic uncertainties have a significant dependence on the reconstructed $t\bar{t}$ mass which is fully taken into account in the analysis. Furthermore, Appendix D contains the acceptance times efficiency values for the different signal mass points used, together with the associated total systematic uncertainty.

[9] The additional b-tagging uncertainty is an extrapolation of the uncertainty from regions of lower p_{T}, and it is approximately 12% for b-jets and 17% for c-jets, added in quadrature to the uncertainty on the jet efficiency correction factor for the 140–200 GeV region.

Table 1: Average impact of the dominant systematic uncertainties on the total background yield and on the estimated yield of a Z' with $m = 1.5$ TeV. The electron and muon channel spectra are added. The shift is given in percent of the nominal value. Certain systematic uncertainties are not applicable to the Z' samples, which is indicated with a bar (−) in the table.

Systematic Uncertainties	Resolved selection yield impact [%] total bkg.	Resolved selection yield impact [%] Z'	Boosted selection yield impact [%] total bkg.	Boosted selection yield impact [%] Z'
Luminosity	2.9	4	3.3	4
PDF	2.9	5	6	2.9
ISR/FSR	0.2	–	0.7	–
Parton shower and fragm.	5	–	4	–
$t\bar{t}$ normalization	8	–	9	–
$t\bar{t}$ EW virtual correction	2.2	–	4	–
$t\bar{t}$ Generator	1.5	–	1.6	–
W+jets $b\bar{b}$+$c\bar{c}$+c vs. light	0.8	–	1.0	–
W+jets $b\bar{b}$ variation	0.2	–	0.4	–
W+jets c variation	1.1	–	0.6	–
W+jets normalization	2.1	–	1.0	–
Multi-Jet norm, e+jets	0.6	–	0.3	–
Multi-Jet norm, μ+jets	1.8	–	0.3	–
JES, small-radius jets	6	2.2	0.7	0.5
JES+JMS, large-radius jets	0.3	4	17	3.3
Jet energy resolution	1.6	0.4	0.6	0.7
Jet vertex fraction	1.7	2.3	2.1	2.4
b-tag efficiency	4	1.8	3.4	6
c-tag efficiency	1.4	0.3	0.7	0.9
Mistag rate	0.7	0.3	0.7	0.1
Electron efficiency	1.0	1.1	1.0	1.0
Muon efficiency	1.5	1.5	1.6	1.6
All systematic uncertainties	14	9	22	9

9 Comparison between data and expected background

After all event selection criteria are applied, 280251 resolved and 5122 boosted events remain. The event yields from data and from the expected backgrounds are listed in Table 2, along with the normalization uncertainties. The full treatment of systematic uncertainties was described in Sec. 8.

Good agreement is observed between the data and the expected background. Figures 3 and 4 show the transverse momentum of the leading (small-radius) jet after the full resolved selection and the transverse momentum of the selected large-radius jet after the boosted selection, respectively. In Figures 5 and 6, the reconstructed mass of the semi-leptonically and hadronically decaying top quark candidates are shown, using the boosted event selection. Figure 7 shows the distribution of the first k_t splitting scale of the selected large-radius jet.

The $t\bar{t}$ invariant mass spectra for the resolved and the boosted selections in the electron and muon channels are shown in Figure 8. Figure 9 shows the $t\bar{t}$ invariant mass spectrum for all channels added together. Data agrees with the expected background within the uncertainties. The slight shape mismatch between data and the expected background that can be seen especially for the resolved selection is fully covered by the uncertainties. Systematic uncertainties which tilt the shape in this way are, e.g., the $t\bar{t}$ generator uncertainty, electroweak virtual corrections, the small-radius jet scale and resolution uncertainties and the ISR/FSR modeling. All of them are significant uncertainties in this analysis.

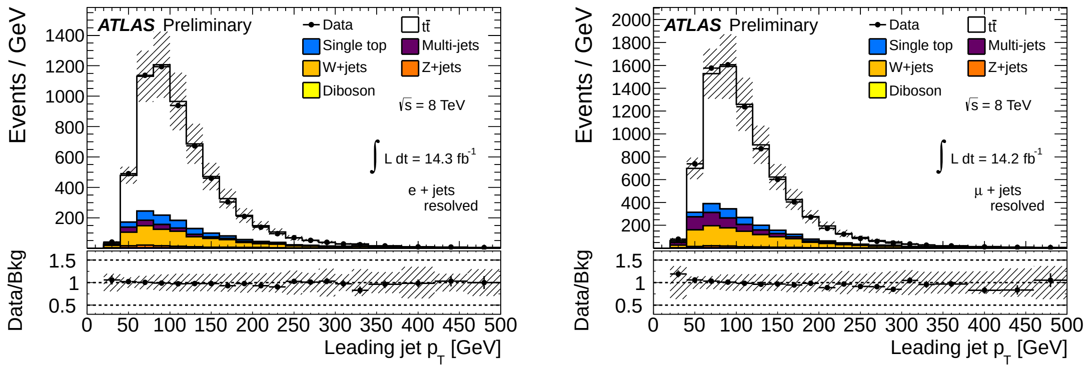

(a) e+jets channel.

(b) μ+jets channel.

Figure 3: The transverse momentum of the leading jet, after the resolved selection. The shaded areas indicate the total systematic uncertainties. Some background sources are too small to be visible in the figure.

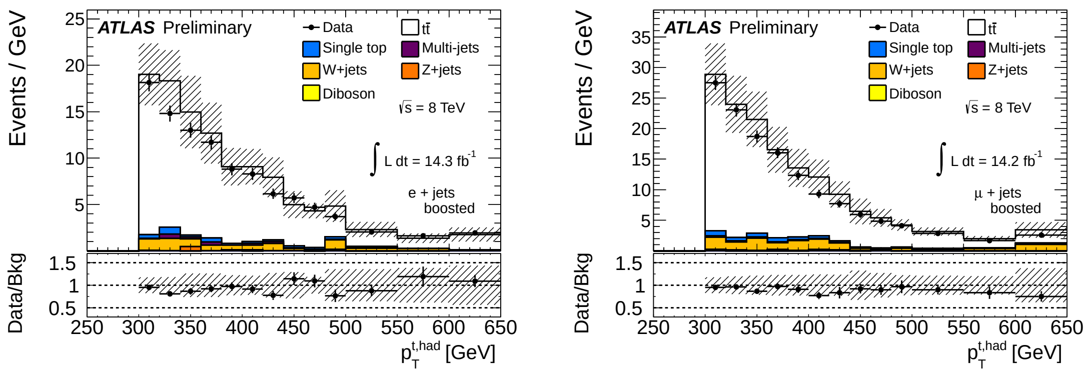

(a) e+jets channel.

(b) μ+jets channel.

Figure 4: The transverse momentum of the hadronically decaying top quark candidate, after the boosted selection. The shaded areas indicate the total systematic uncertainties. Some background sources are too small to be visible in the figure. The last bin in each histogram includes overflow events.

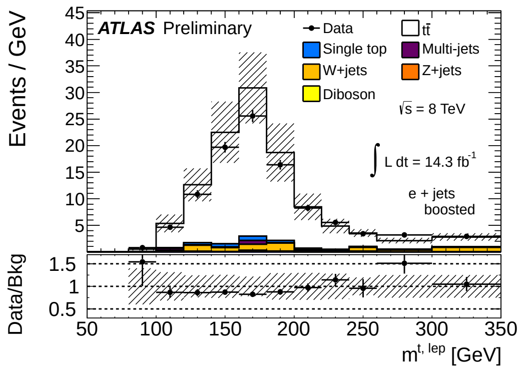

(a) e+jets channel.

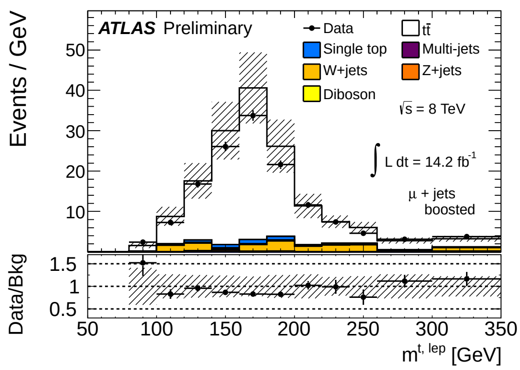

(b) μ+jets channel.

Figure 5: The invariant mass of the semi-leptonically decaying top quark candidate, $m^{t,\,\mathrm{lep}}$, after the boosted selection. The mass has been reconstructed from the narrow jet, the charged lepton and the missing transverse momentum, using a W mass constraint to obtain the longitudinal momentum of the neutrino. The shaded areas indicate the total systematic uncertainties. Some background sources are too small to be visible in the figure.

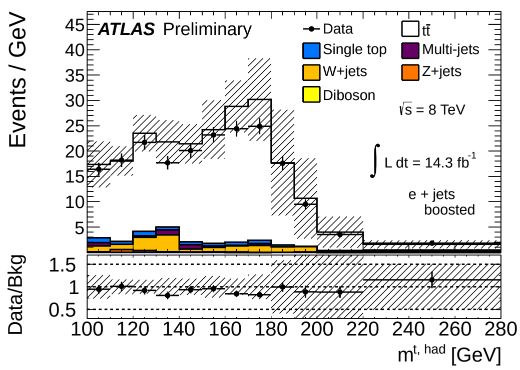

(a) e+jets channel.

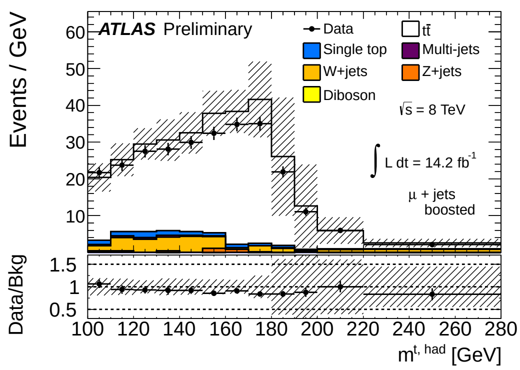

(b) μ+jets channel.

Figure 6: The mass of the hadronic top jet, $m^{t,\,\mathrm{had}}$, after the boosted selection. The shaded areas indicate the total systematic uncertainties. Some background sources are too small to be visible in the figure.

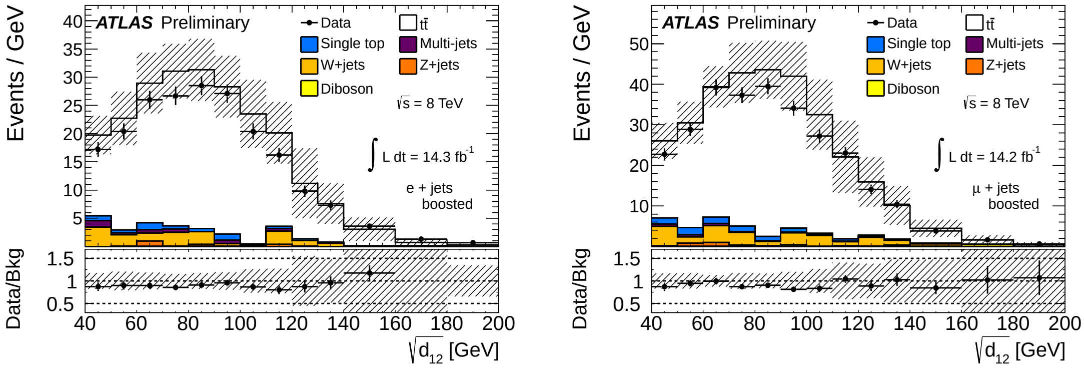

(a) e+jets channel.

(b) μ+jets channel.

Figure 7: The first k_t splitting scale, $\sqrt{d_{12}}$, of the hadronic top jet after the boosted selection. The shaded areas indicate the total systematic uncertainties. Some background sources are too small to be visible in the figure.

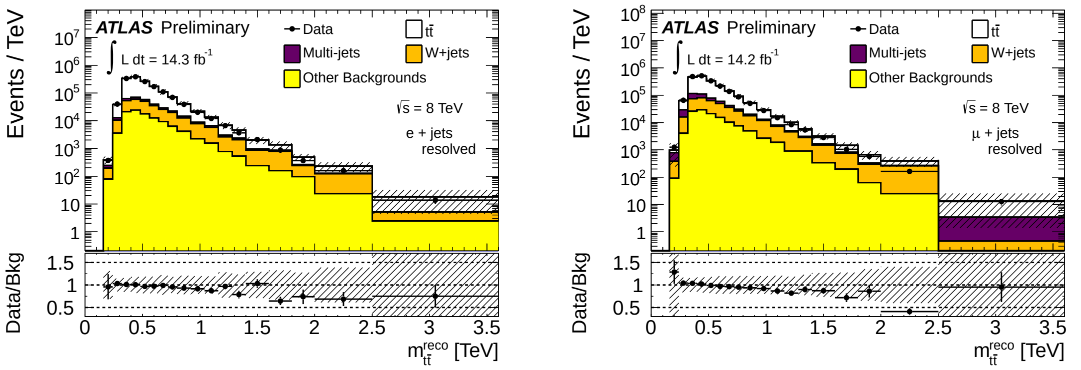

(a) e+jets channel, resolved selection.

(b) μ+jets channel, resolved selection.

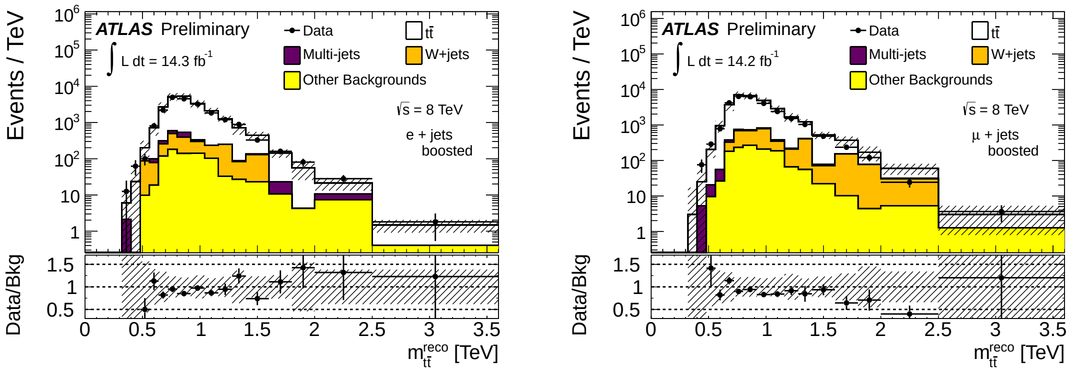

(c) e+jets channel, boosted selection.

(d) μ+jets channel, boosted selection.

Figure 8: The $t\bar{t}$ invariant mass spectra for the two channels and the two selection methods. The shaded areas indicate the total systematic uncertainties.

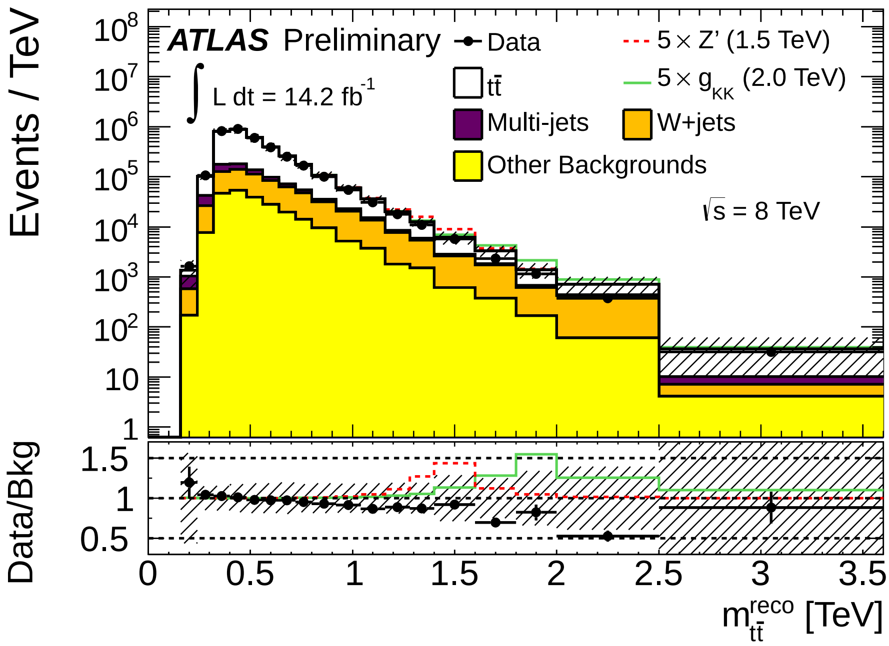

Figure 9: The $t\bar{t}$ invariant mass spectrum, summing the spectra from the two channels and the two selection methods. The shaded areas indicate the total systematic uncertainties. Two benchmark signals are indicated on top of the background, a Z' with $m = 1.5$ TeV and a g_{KK} with $m = 2.0$ TeV. The assumed cross sections of the signals in this figure are the theoretical predictions given in Tables 3 and 4.

Table 2: Data and expected background event yields after the resolved and boosted selections. The uncertainty on the normalization of the expected backgrounds yield is listed.

	Resolved selection		
Type	e+jets	μ+jets	Sum
$t\bar{t}$	94000 ± 15000	118000 ± 19000	211000 ± 33000
Single top	6800 ± 800	8400 ± 1100	15200 ± 1900
Multi-jet	3700 ± 1800	10000 ± 5000	14000 ± 6000
W+jets	16000 ± 4000	23000 ± 6000	39000 ± 10000
Z+jets	1800 ± 400	1800 ± 400	3600 ± 800
Di-bosons	230 ± 50	320 ± 60	550 ± 100
Total	121000 ± 17000	162000 ± 23000	283000 ± 39000
Data	119490	160878	280251
	Boosted selection		
Type	e+jets	μ+jets	Sum
$t\bar{t}$	2100 ± 500	2800 ± 600	4900 ± 1100
Single top	71 ± 15	105 ± 22	176 ± 34
Multi-jet	39 ± 19	32 ± 16	71 ± 25
W+jets	170 ± 60	310 ± 90	480 ± 140
Z+jets	18 ± 11	33 ± 8	52 ± 15
Di-bosons	2.0 ± 0.8	1.5 ± 1.4	3.5 ± 1.8
Total	2400 ± 500	3300 ± 700	5600 ± 1200
Data	2177	2945	5122

10 Results

After the reconstruction of the $t\bar{t}$ mass spectra, the data and expected background distributions are compared using BumpHunter [82], which is a hypothesis testing tool that searches the data for local excesses or deficits compared to the expected background, taking the look-elsewhere effect into account over the full mass spectrum. The background templates used by the BumpHunter are taken from the Monte-Carlo and data-determined distributions. After accounting for the systematic uncertainties, no significant deviation from the expected background is found. Hence upper limits are set on the cross section times branching ratio of the Z' and KK gluon benchmark models using a Bayesian technique, implemented in a tool developed by the DØ collaboration [83]. At each mass point, the prior is taken to be constant with the signal cross section. The Bayesian limits are in good agreement with results obtained using the CL_s method [84]. For each of the models investigated, 95% CL upper limits are set on the product of production cross section and branching ratio into $t\bar{t}$.

Upper cross section limits are given for the two benchmark models for the combination of the two selections (see Figure 10). The numerical values of the upper cross section limits are given in Table 3 (Z') and Table 4 (g_{KK}). In the combination, the four statistically uncorrelated spectra are used, corresponding to boosted and resolved selections, as well as e+jets and μ+jets decay channels. Using the combined upper cross section limits, a leptophobic topcolor Z' boson (KK gluon) with mass between 0.5 and 1.8 TeV (0.5 and 2.0 TeV) is excluded at 95% CL, while the expected exclusion range is between 0.5 and 1.9 TeV (0.5 and 2.1 TeV).

The boosted analysis has the higher signal efficiency, while the resolved has a much larger non-resonant component. Thus the small deficit at high mass in the resolved distributions favours values

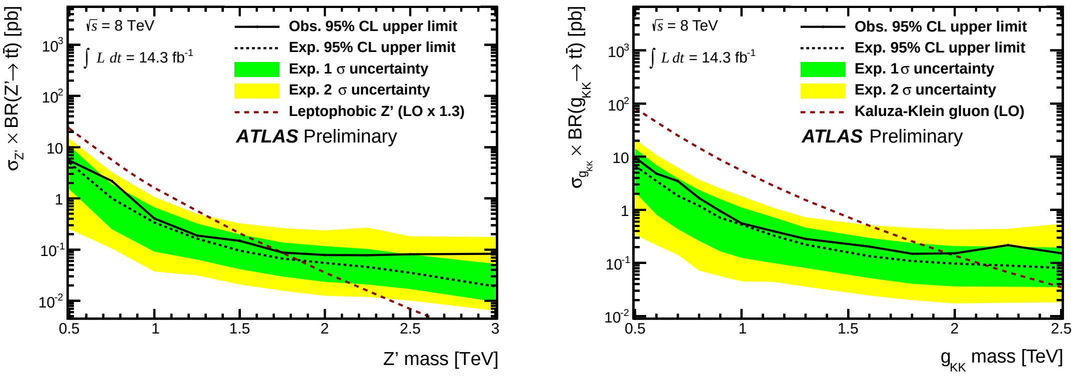

(a) Z' upper cross section limits.

(b) g_{KK} upper cross section limits.

Figure 10: Observed and expected upper cross section limits times the $t\bar{t}$ branching ratio on (a) Z' bosons and (b) Kaluza–Klein gluons. The resolved and the boosted selections have been combined in the estimation of the limits. Both systematic and statistical uncertainties are included.

of the nuisance parameters which decrease the estimated high-mass background in all channels and the small excess in the boosted electron channel is amplified, leading to weaker observed limits than expected limits.

Table 3: Upper 95% CL cross section limits times branching ratio on a leptophobic topcolor Z' decaying to $t\bar{t}$, using the combination of all four samples. The observed and expected limits for each mass point are given, as well as the $\pm 1\sigma$ variation of the expected limit. The second column gives the theoretical predictions with the 1.3 K-factor to account for NLO effects.

Mass (TeV)	$\sigma\times$ BR $\times 1.3$ [pb]	Obs. (pb)	Exp. (pb)	-1σ (pb)	$+1\sigma$ (pb)
0.50	23.	5.30	4.99	1.50	10.7
0.75	5.6	2.17	1.00	0.249	1.87
1.00	1.6	0.406	0.335	0.091	0.674
1.25	0.57	0.187	0.160	0.064	0.323
1.50	2.1×10^{-1}	0.148	0.096	0.041	0.198
1.75		0.087	0.066	0.030	0.137
2.00	3.9×10^{-2}	0.078	0.055	0.023	0.117
2.25		0.078	0.045	0.021	0.103
2.50	6.9×10^{-3}	0.081	0.035	0.017	0.081
3.00	1.5×10^{-3}	0.083	0.019	0.010	0.053

11 Summary

A search for $t\bar{t}$ resonances in the lepton plus jets decay channel has been carried out with the ATLAS experiment at the LHC. The search uses a data sample corresponding to an integrated luminosity of 14.3 fb^{-1} of proton-proton collisions at a center-of-mass energy of 8 TeV. The $t\bar{t}$ system is reconstructed in two different ways. For the resolved selection, the hadronic top quark decay is reconstructed as two or three $R = 0.4$ jets, and for the boosted selection, it is reconstructed as one $R = 1.0$ jet. No excess

Table 4: Upper 95% CL cross section limits times branching ratio on a Kaluza–Klein gluon decaying to $t\bar{t}$, combined samples. The observed and expected limits for each mass point are given, as well as the $\pm 1\sigma$ variation of the expected limit. The second column gives the theoretical predictions.

Mass (TeV)	$\sigma\times$ BR [pb]	Obs. (pb)	Exp. (pb)	-1σ (pb)	$+1\sigma$ (pb)
0.50	82.	9.62	6.73	2.15	14.1
0.60	45.	4.79	3.48	0.813	6.98
0.70	25.	3.48	1.84	0.436	3.90
0.80	15.	1.66	1.19	0.262	2.37
0.90	8.8	0.948	0.711	0.165	1.60
1.00	5.5	0.561	0.529	0.125	1.11
1.15	2.8	0.394	0.329	0.100	0.720
1.30	1.5	0.282	0.221	0.081	0.464
1.60	0.50	0.204	0.134	0.052	0.296
1.80	0.26	0.149	0.109	0.041	0.237
2.00	0.14	0.153	0.097	0.036	0.209
2.25	0.067	0.218	0.089	0.036	0.203
2.50	0.035	0.152	0.080	0.035	0.196

of events beyond the Standard Model backgrounds is observed in the $t\bar{t}$ invariant mass spectrum. Upper cross section times branching ratio limits are set on two benchmark models: a narrow Z' boson from Ref. [1] and a broad Randall–Sundrum Kaluza–Klein gluon from Ref. [3]. The 95% CL upper cross section limits for the narrow resonance range from 5.3 pb at a resonance mass of 0.5 TeV to 0.08 pb at 3 TeV. The upper cross section limits determined for the broad resonance are higher, 9.6 pb (0.152 pb) at 0.5 (3.0) TeV. Based on these results, the existence of the narrow leptophobic topcolor Z' in the range 0.5 TeV $< m_{Z'} <$ 1.8 TeV is excluded at 95% CL, the expected exclusion range is 0.5 TeV $< m_{Z'} <$1.9 TeV. A broad Kaluza–Klein gluon with mass between 0.5 TeV and 2.0 TeV is also excluded at 95% CL, the expected exclusion range is 0.5 TeV $< m_{g_{\rm KK}} <$2.1 TeV.

References

[1] C. T. Hill, *Topcolor assisted technicolor*, Phys. Lett. **B345** (1995) 483–489, `arXiv:9411426 [hep-ph]`.

C. T. Hill and S. J. Parke, *Top production: Sensitivity to new physics*, Phys. Rev. **D49** (1994) 4454–4462, `arXiv:9312324 [hep-ph]`.

[2] P. H. Frampton and S. L. Glashow, *Chiral Color: An Alternative to the Standard Model*, Phys. Lett. **B190** (1987) 157–161.

R. M. Godbole and D. Choudhury, *Nonstandard, strongly interacting spin one $t\bar{t}$ resonances*, Proceedings of the 34th International Conference on High Energy Physics (ICHEP 2008) (2008) , `arXiv:0810.3635 [hep-ph]`.

[3] B. Lillie, L. Randall, and L.-T. Wang, *The Bulk RS KK-gluon at the LHC*, JHEP **0709** (2007) 074, `arXiv:0701166 [hep-ph]`.

[4] B. Lillie, J. Shu, and T. M. P. Tait, *Kaluza-Klein Gluons as a Diagnostic of Warped Models*, Phys. Rev. D **76** (2007) 115016, `arXiv:0706.3960 [hep-ph]`.

[5] K. Agashe, A. Belyaev, T. Krupovnickas, G. Perez, and J. Virzi, *LHC signals from warped extra dimensions*, Phys. Rev. D **77** (2008) 015003, `arXiv:0612015 [hep-ph]`.

[6] A. Djouadi, G. Moreau, and R. K. Singh, *Kaluza-Klein excitations of gauge bosons at the LHC*, Nucl. Phys. **B797** (2008) 1–26, `arXiv:0706.4191 [hep-ph]`.

[7] K. Agashe, H. Davoudiasl, G. Perez, and A. Soni, *Warped Gravitons at the LHC and Beyond*, Phys. Rev. D **76** (2007) 036006, `arXiv:0701186 [hep-ph]`.

[8] R. M. Harris, C. T. Hill, and S. J. Parke, *Cross section for topcolor $Z'(t)$ decaying to $t\bar{t}$*, `arXiv:9911288 [hep-ph]`.

R. M. Harris and S. Jain, *Cross Sections for Leptophobic Topcolor Z' Decaying to Top-Antitop*, Eur. Phys. J. **C72** (2012) 2072, `arXiv:1112.4928 [hep-ph]`.

[9] D0 Collaboration, V. Abazov et al., *Search for $t\bar{t}$ resonances in the lepton plus jets final state in $p\bar{p}$ collisions at $\sqrt{s}$ = 1.96 TeV*, Phys. Lett. **B668** (2008) 98–104, `arXiv:0804.3664 [hep-ex]`.

[10] CDF Collaboration, T. Aaltonen et al., *Search for resonant $t\bar{t}$ production in $p\bar{p}$ collisions at $\sqrt{s}$ = 1.96 TeV*, Phys. Rev. Lett. **100** (2008) 231801, `arXiv:0709.0705 [hep-ex]`.

[11] J. Pumplin et al., *New generation of parton distributions with uncertainties from global QCD analysis*, JHEP **0207** (2002) 012, `arXiv:0201195 [hep-ph]`.

[12] ATLAS Collaboration, *A search for $t\bar{t}$ resonances with the ATLAS detector in 2.05 fb^{-1} of proton-proton collisions at $\sqrt{s}$ = 7 TeV*, Eur. Phys. J. **C72** (2012) 2083, `arXiv:1205.5371 [hep-ex]`.

[13] ATLAS Collaboration, *A search for $t\bar{t}$ resonances in lepton+jets events with highly boosted top quarks collected in pp collisions at $\sqrt{s}$ = 7 TeV with the ATLAS detector*, JHEP **1209** (2012) 041, `arXiv:1207.2409 [hep-ex]`.

[14] CMS Collaboration, *Search for anomalous $t\bar{t}$ production in the highly-boosted all-hadronic final state*, JHEP **1209** (2012) 029, `arXiv:1204.2488 [hep-ex]`.

[15] CMS Collaboration, *Search for resonant $t\bar{t}$ production in lepton+jets events in pp collisions at $\sqrt{s}$ = 7 TeV*, JHEP **1212** (2012) 015, `arXiv:1209.4397 [hep-ex]`.

[16] CMS Collaboration, *Search for Z ' resonances decaying to $t\bar{t}$ in dilepton+jets final states in pp collisions at $\sqrt{s}$ = 7 TeV*, `arXiv:1211.3338 [hep-ex]`.

[17] ATLAS Collaboration, *A search for $t\bar{t}$ resonances in the lepton plus jets final state using 4.66 fb^{-1} of pp collisions at sqrt(s) = 7 TeV*, ATLAS-CONF-2012-136 (2012). https://cds.cern.ch/record/1478974.

[18] CMS Collaboration, *Search for $t\bar{t}$ resonances in semileptonic final state*, CMS-PAS-B2G-12-006 (2013). https://cds.cern.ch/record/1543467.

[19] J. Gao, C. S. Li, B. H. Li, C.-P. Yuan, and H. X. Zhu, *Next-to-leading order QCD corrections to the heavy resonance production and decay into top quark pair at the LHC*, Phys. Rev. **D82** (2010) 014020, `arXiv:1004.0876 [hep-ph]`.

[20] F. Caola, K. Melnikov, and M. Schulze, *A complete next-to-leading order QCD description of resonant Z' production and decay into $t\bar{t}$ final states*, Phys. Rev. **D87** (2013) 034015, `arXiv:1211.6387 [hep-ph]`.

[21] ATLAS Collaboration, *Prospects for top anti-top resonance searches using early ATLAS data*, ATL-PHYS-PUB-2010-008 (2010). https://cdsweb.cern.ch/record/1278454.

[22] J. Alwall et al., *MadGraph/MadEvent v4: The New Web Generation*, JHEP **0709** (2007) 028, `arXiv:0706.2334 [hep-ph]`.

[23] CDF Collaboration, T. Aaltonen et al. , *A search for resonant production of $t\bar{t}$ pairs in* 4.8 fb^{-1} *of integrated luminosity of $p\bar{p}$ collisions at* $\sqrt{s}$ = 1.96 TeV, Phys. Rev. D **84** (2011) 072004, `arXiv:1107.5063 [hep-ex]`.

CDF Collaboration, T. Aaltonen et al. , *Search for resonant production of $t\bar{t}$ decaying to jets in $p\bar{p}$ collisions at $\sqrt{s}$ = 1.96 TeV*, Phys. Rev. D **84** (2011) 072003, `arXiv:1108.4755 [hep-ex]`.

CDF Collaboration, T. Aaltonen et al., *Search for resonant top-antitop production in the semi-leptonic decay mode using the full CDF data set*, `arXiv:1211.5363 [hep-ex]`.

[24] D0 Collaboration, V. Abazov et al., *Search for a narrow $t\bar{t}$ resonance in $p\bar{p}$ collisions at $\sqrt{s}$ = 1.96 TeV*, Phys. Rev. D **85** (2012) 051101, `arXiv:1111.1271 [hep-ex]`.

[25] D. Krohn, J. Thaler, and L.-T. Wang, *Jet Trimming*, JHEP **1002** (2010) 084, `arXiv:0912.1342 [hep-ph]`.

[26] ATLAS Collaboration, *The ATLAS Experiment at the CERN Large Hadron Collider*, JINST **3** (2008) S08003.

[27] ATLAS Collaboration, *Luminosity Determination in pp Collisions at $\sqrt{s}$ = 7 TeV Using the ATLAS Detector at the LHC*, Eur. Phys. J. **C71** (2011) 1630, `arXiv:1101.2185 [hep-ex]`.

[28] ATLAS Collaboration, *Improved luminosity determination in pp collisions at $\sqrt{s}$ = 7 TeV using the ATLAS detector at the LHC*, `arXiv:1302.4393 [hep-ex]`.

[29] GEANT4 Collaboration, S. Agostinelli et al., *GEANT4: A simulation toolkit*, Nucl. Instrum. Meth. **A506** (2003) 250–303.

[30] ATLAS Collaboration, *The ATLAS Simulation Infrastructure*, Eur. Phys. J. **C70** (2010) 823–874, `arXiv:1005.4568 [physics.ins-det]`.

[31] S. Frixione and B. R. Webber, *Matching NLO QCD computations and parton shower simulations*, JHEP **0206** (2002) 029, `arXiv:0204244 [hep-ph]`.

[32] S. Frixione, P. Nason, and B. R. Webber, *Matching NLO QCD and parton showers in heavy flavor production*, JHEP **0308** (2003) 007, `arXiv:0305252 [hep-ph]`.

[33] S. Frixione, F. Stoeckli, P. Torrielli, B. R. Webber, and C. D. White, *The MC@NLO 4.0 Event Generator*, `arXiv:1010.0819 [hep-ph]`.

[34] G. Corcella et al., *HERWIG 6: An Event generator for hadron emission reactions with interfering gluons (including supersymmetric processes)*, JHEP **0101** (2001) 010, `arXiv:0011363 [hep-ph]`.

G. Corcella et al., *HERWIG 6.5 release note*, `arXiv:0210213 [hep-ph]`.

[35] J. M. Butterworth, J. R. Forshaw, and M. H. Seymour, *Multiparton interactions in photoproduction at HERA*, Z. Phys. **C72** (1996) 637–646, `arXiv:9601371 [hep-ph]`.

[36] H.-L. Lai et al., *New parton distributions for collider physics*, Phys. Rev. D **82** (2010) 074024, arXiv:1007.2241 [hep-ph].

[37] M. Beneke, M. Czakon, P. Falgari, A. Mitov, and C. Schwinn, *Threshold expansion of the $gg(q\bar{q}) \to Q\bar{Q} + X$ cross section at $O(\alpha_S^4)$*, Phys. Lett. **B690** (2010) 483–490, arXiv:0911.5166 [hep-ph].

[38] M. Aliev et al., *HATHOR: HAdronic Top and Heavy quarks crOss section calculatoR*, Comp. Phys. Comm. **182** (2011) 1034–1046, arXiv:1007.1327 [hep-ph].

[39] S. Frixione, E. Laenen, P. Motylinski, and B. R. Webber, *Single-top production in MC@NLO*, JHEP **0603** (2006) 092, arXiv:0512250 [hep-ph].

[40] S. Frixione et al., *Single-top hadroproduction in association with a W boson*, JHEP **0807** (2008) 029, arXiv:0805.3067 [hep-ph].

[41] B. P. Kersevan and E. Richter-Was, *The Monte Carlo event generator AcerMC version 2.0 with interfaces to PYTHIA 6.2 and HERWIG 6.5*, arXiv:0405247 [hep-ph].

[42] T. Sjöstrand, S. Mrenna, and P. Z. Skands, *PYTHIA 6.4 Physics and Manual*, JHEP **0605** (2006) 026, arXiv:0603175 [hep-ph].

[43] N. Kidonakis, *Next-to-next-to-leading-order collinear and soft gluon corrections for t-channel single top quark production*, Phys. Rev. D **83** (2011) 091503, arXiv:1103.2792 [hep-ph].

[44] N. Kidonakis, *Two-loop soft anomalous dimensions for single top quark associated production with a W- or H-*, Phys. Rev. D **82** (2010) 054018, arXiv:1005.4451 [hep-ph].

[45] N. Kidonakis, *NNLL resummation for s-channel single top quark production*, Phys. Rev. D **81** (2010) 054028, arXiv:1001.5034 [hep-ph].

[46] M. L. Mangano et al., *ALPGEN, a generator for hard multiparton processes in hadronic collisions*, JHEP **0307** (2003) 001, arXiv:0206293 [hep-ph].

[47] J. Alwall et al., *Comparative study of various algorithms for the merging of parton showers and matrix elements in hadronic collisions*, Eur. Phys. J. **C53** (2008) 473–500, arXiv:0706.2569 [hep-ph].

[48] R. Hamberg, W. van Neerven, and T. Matsuura, *A Complete calculation of the order α_s^2 correction to the Drell-Yan K factor*, Nucl. Phys. **B359** (1991) 343–405.

[49] R. Gavin, Y. Li, F. Petriello, and S. Quackenbush, *W Physics at the LHC with FEWZ 2.1*, arXiv:1201.5896 [hep-ph].

[50] ATLAS Collaboration, *Measurement of the top quark-pair production cross section with ATLAS in pp collisions at $\sqrt{s} = 7$ TeV*, Eur. Phys. J. **C71** (2011) 1577, arXiv:1012.1792 [hep-ex].

[51] P. Langacker, *The Physics of Heavy Z' Gauge Bosons*, Rev. Mod. Phys. **81** (2009) 1199–1228, arXiv:0801.1345 [hep-ph].

[52] T. Sjostrand, S. Mrenna, and P. Z. Skands, *A Brief Introduction to PYTHIA 8.1*, Comput. Phys. Commun. **178** (2008) 852–867, arXiv:0710.3820 [hep-ph].

[53] A. Martin, W. Stirling, R. Thorne, and G. Watt, *Parton distributions for the LHC*, Eur. Phys. J. **C63** (2009) 189–285, arXiv:0901.0002 [hep-ph].

[54] M. Cacciari, G. P. Salam, and G. Soyez, *The Anti-k(t) jet clustering algorithm*, JHEP **0804** (2008) 063, arXiv:0802.1189 [hep-ph].

M. Cacciari, G. P. Salam, and G. Soyez, *FastJet user manual*, Eur. Phys. J. **C 72** (2012) 1896, arXiv:1111.6097 [hep-ph].

[55] W. Lampl et al., *Calorimeter clustering algorithms: Description and performance*, ATL-LARG-PUB-2008-002 (2008). https://cdsweb.cern.ch/record/1099735.

[56] Ç. İşsever, K. Borras, and D. Wegener, *An improved weighting algorithm to achieve software compensation in a fine grained LAr calorimeter*, Nucl. Instr. and Meth. **A545** (2005) 803–812, arXiv:0408129 [physics].

[57] T. Barillari et al., *Local hadronic calibration*, ATL-LARG-PUB-2009-001-2 (2009). https://cdsweb.cern.ch/record/1112035.

[58] ATLAS Collaboration, *Jet energy measurement with the ATLAS detector in proton-proton collisions at $\sqrt{s}$ = 7 TeV*, Eur. Phys. J. **C73** (2013) 2304, arXiv:1112.6426 [hep-ex].

[59] ATLAS Collaboration, *Studies of the impact and mitigation of pile-up on large-R and groomed jets in ATLAS at $\sqrt{s}$ = 7 TeV*, ATLAS-CONF-2012-066 (2012). https://cdsweb.cern.ch/record/1459531.

[60] S. D. Ellis and D. E. Soper, *Successive combination jet algorithm for hadron collisions*, Phys. Rev. D **48** (1993) 3160–3166, arXiv:9305266 [hep-ph].

[61] ATLAS Collaboration, *Performance of large-R jets and jet substructure reconstruction with the ATLAS detector*, ATLAS-CONF-2012-065 (2012). https://cdsweb.cern.ch/record/1459530.

[62] ATLAS Collaboration, *Jet energy scale and its systematic uncertainty in proton-proton collisions at sqrt(s)=7 TeV with ATLAS 2011 data*, ATLAS-CONF-2012-004 (2013). https://cds.cern.ch/record/1509552.

[63] ATLAS Collaboration, *Measurement of the b-tag Efficiency in a Sample of Jets Containing Muons with 5 fb^{-1} of Data from the ATLAS Detector*, ATLAS-CONF-2012-043 (2012). https://cdsweb.cern.ch/record/1435197.

[64] ATLAS Collaboration, *Electron performance measurements with the ATLAS detector using the 2010 LHC proton-proton collision data*, Eur. Phys. J. **C72** (2012) 1909, arXiv:1110.3174 [hep-ex].

[65] K. Rehermann and B. Tweedie, *Efficient Identification of Boosted Semileptonic Top Quarks at the LHC*, JHEP **1103** (2011) 059, arXiv:1007.2221 [hep-ph].

[66] ATLAS Collaboration, *Performance of Missing Transverse Momentum Reconstruction in Proton-Proton Collisions at 7 TeV with ATLAS*, Eur. Phys. J. **C72** (2012) 1844, arXiv:1108.5602 [hep-ex].

[67] ATLAS Collaboration, *Measurement of the t-channel single top-quark production cross section in pp collisions at $\sqrt{s}$ = 7 TeV with the ATLAS detector*, Phys. Lett. B **717** (2012) 330–350, arXiv:1205.3130 [hep-ex].

[68] ATLAS Collaboration, *Measurement of the charge asymmetry in top quark pair production in pp collisions at $\sqrt{s}$ = 7 TeV using the ATLAS detector*, Eur. Phys. J. **C72** (2012) 2039, arXiv:1203.4211 [hep-ex].

[69] ATLAS Collaboration, *Measurements of top quark pair relative differential cross-sections with ATLAS in pp collisions at $\sqrt{s}$ = 7 TeV*, Eur. Phys. J. **C73** (2013) 2261, arXiv:1207.5644 [hep-ex].

[70] ATLAS Collaboration, *Measurement of the top quark pair production cross-section with ATLAS in the single lepton channel*, Phys. Lett. **B711** (2012) 244–263, arXiv:1201.1889.

[71] A. Martin, W. Stirling, R. Thorne, and G. Watt, *Uncertainties on α_S in global PDF analyses and implications for predicted hadronic cross sections*, Eur. Phys. J. **C64** (2009) 653–680, arXiv:0905.3531 [hep-ph].

[72] M. Cacciari et al., *Top-pair production at hadron colliders with next-to-next-to-leading logarithmic soft-gluon resummation*, Phys. Lett. **B710** (2012) 612–622, arXiv:1111.5869 [hep-ph].

[73] M. Czakon and A. Mitov, *Top++: A Program for the Calculation of the Top-Pair Cross-Section at Hadron Colliders*, arXiv:1112.5675 [hep-ph].

[74] ATLAS Collaboration, *Luminosity Determination in pp Collisions at $\sqrt{s}$ = 7 TeV using the ATLAS Detector in 2011*, ATLAS-CONF-2011-116 (2011) . http://cds.cern.ch/record/1376384.

[75] A. V. Manohar and M. Trott, *Electroweak Sudakov Corrections and the Top Quark Forward-Backward Asymmetry*, Phys. Lett. **B711** (2012) 313–316, arXiv:1201.3926 [hep-ph].

[76] R. D. Ball et al., *Parton distributions with LHC data*, Nucl. Phys. **B867** (2013) 244–289, arXiv:1207.1303 [hep-ph].

[77] M. Botje et al., *The PDF4LHC Working Group Interim Recommendations*, arXiv:1101.0538 [hep-ph].

[78] ATLAS Collaboration, *Jet mass and substructure of inclusive jets in $\sqrt{s}$ = 7 TeV pp collisions with the ATLAS experiment*, JHEP **1205** (2012) 128, arXiv:1203.4606 [hep-ex].

[79] ATLAS Collaboration, *Measurement of the Mistag Rate with 5 fb^{-1} of Data Collected by the ATLAS Detector*, ATLAS-CONF-2012-040 (2012) . https://cdsweb.cern.ch/record/1435194.

[80] ATLAS Collaboration, *Measurement of $t\bar{t}$ production with a veto on additional central jet activity in pp collisions at sqrt(s) = 7 TeV using the ATLAS detector*, Eur. Phys. J. **C72** (2012) 2043, arXiv:1203.5015 [hep-ex].

[81] S. Frixione, P. Nason, and C. Oleari, *Matching NLO QCD computations with Parton Shower simulations: the POWHEG method*, JHEP **0711** (2007) 070, arXiv:0709.2092 [hep-ph].

[82] G. Choudalakis, *On hypothesis testing, trials factor, hypertests and the BumpHunter*, arXiv:1101.0390 [physics.data-an].

[83] I. Bertram et al., *A Recipe for the construction of confidence limits*, FERMILAB-TM-2104 (2000).

[84] T. Junk, *Confidence level computation for combining searches with small statistics*, Nucl. Instrum. Meth. **A 434** (1999) 435–443, arXiv:9902006 [hep-ex].

A. L. Read, *Presentation of search results: The CL(s) technique*, J. Phys. **G 28** (2002) 2693–2704.

A Performance of mini-isolation

The signal efficiency versus false-identification rate of various lepton isolation discriminants is shown in Figure 11. The false-identification rate is evaluated from data, using a multi-jet dominated sample with similar event topology. The adopted selection of $I_{\mathrm{mini}}/p_{\mathrm{T}} < 0.05$ gives a false-identification rate of 2.2%. Compared to other discriminants at similar operating point, this choice provides highest efficiency, and is very stable when the top becomes highly boosted.

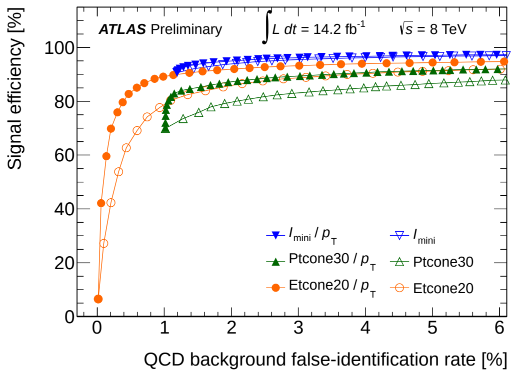

(a) SM $t\bar{t}$

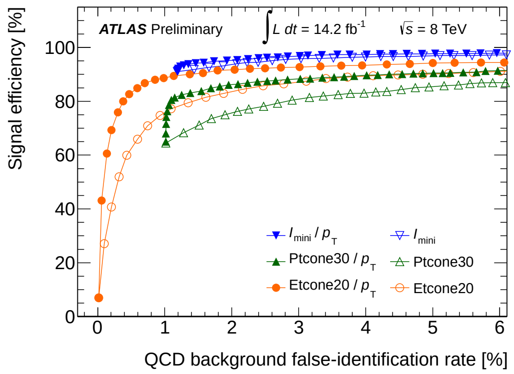

(b) 1.0 TeV Z'

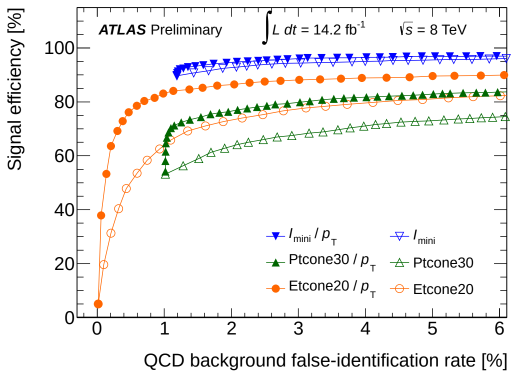

(c) 1.5 TeV Z'

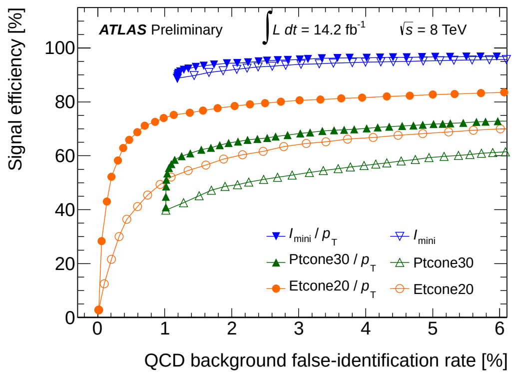

(d) 2.0 TeV Z'

Figure 11: The signal efficiency versus false-identification rate of various lepton isolation discriminants, in the muon channel. The signal efficiency is evaluated from MC of (a) SM $t\bar{t}$ (b) 1.0 TeV Z' (c) 1.5 TeV Z' (d) 2.0 TeV Z', for events passing all the other boosted selections except for isolation.

B Selection efficiency

Various selection efficiencies as a function of the true $m_{t\bar{t}}$ for the Z' resonance are shown in Figure 12. Only the resolved approach can select events at low $m_{t\bar{t}}$, while the boosted selection, which becomes efficient around 1 TeV, is most relevant at very high masses. The fraction of events selected only by the resolved analysis is not negligible, even at high mass. Almost half of these events contain a high-mass jet ($m_{j0.4} > 60$ GeV).

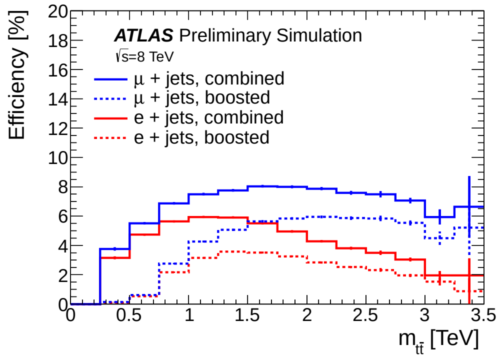

(a) Combined selection and boosted selection.

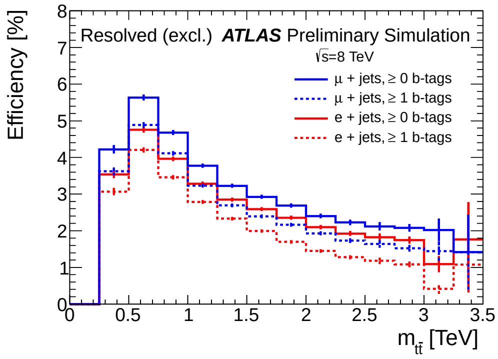

(b) Resolved selection, no overlap with the boosted selection.

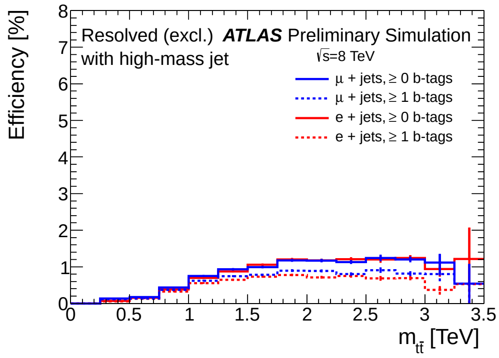

(c) Resolved selection for events with a high-mass jet, not overlapping with the boosted selection.

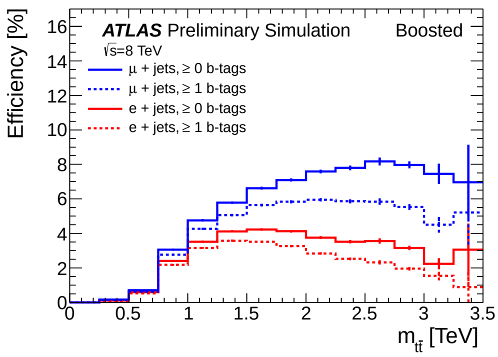

(d) Boosted selection.

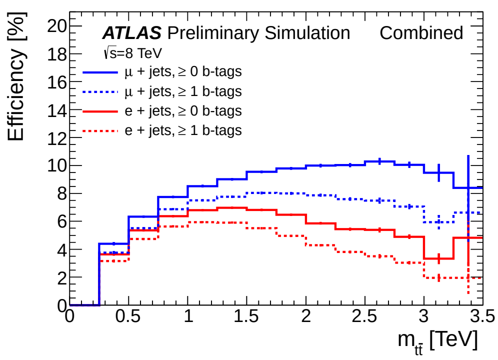

(e) Combination of selections.

Figure 12: Various selection efficiencies as a function of the true $m_{t\bar{t}}$ for the Z' resonance. The μ+jets channel is shown with blue lines and the e+jets channel with red.

C Event display of highly boosted ttbar candidate events from data

Event displays for two events that pass the boosted selection and also fulfill the resolved criteria are shown in Figure 13.

D Acceptance × efficiency for signal

Table 5: Acceptance × efficiency for $Z' \to t\bar{t}$ samples.

Resolved selection acceptance × efficiency		
Z' mass [TeV]	e+jets	μ+jets
0.5	0.029 ± 0.0024	0.033 ± 0.0029
0.75	0.035 ± 0.0026	0.045 ± 0.004
1.0	0.031 ± 0.0025	0.039 ± 0.0029
1.25	0.0273 ± 0.0020	0.032 ± 0.0024
1.5	0.0247 ± 0.0016	0.029 ± 0.0018
1.75	0.0224 ± 0.0015	0.0255 ± 0.0017
2.0	0.0199 ± 0.0011	0.0255 ± 0.0018
2.25	0.0194 ± 0.0012	0.025 ± 0.0022
2.5	0.0183 ± 0.0011	0.0246 ± 0.0019
3.0	0.0194 ± 0.0011	0.0242 ± 0.0019
Boosted selection acceptance × efficiency		
Z' mass [TeV]	e+jets	μ+jets
0.5	0.00023 ± 0.00007	0.00011 ± 0.00004
0.75	0.0055 ± 0.0015	0.0063 ± 0.0020
1.0	0.0203 ± 0.0018	0.0272 ± 0.0023
1.25	0.0292 ± 0.0017	0.039 ± 0.0023
1.5	0.0313 ± 0.0022	0.046 ± 0.004
1.75	0.033 ± 0.004	0.050 ± 0.007
2.0	0.029 ± 0.005	0.053 ± 0.011
2.25	0.027 ± 0.006	0.051 ± 0.013
2.5	0.026 ± 0.006	0.051 ± 0.014
3.0	0.020 ± 0.004	0.045 ± 0.014

Table 6: Acceptance × efficiency for $g_{KK} \to t\bar{t}$ samples.

Resolved selection acceptance × efficiency		
g_{KK} mass [TeV]	e+jets	μ+jets
0.5	0.0277 ± 0.0021	0.0351 ± 0.0029
0.6	0.0327 ± 0.0025	0.0400 ± 0.0032
0.7	0.0340 ± 0.0025	0.0440 ± 0.0032
0.8	0.0350 ± 0.0028	0.0437 ± 0.0035
0.9	0.0313 ± 0.0024	0.0400 ± 0.0032
1.0	0.0300 ± 0.0023	0.0370 ± 0.0028
1.15	0.0281 ± 0.0019	0.0355 ± 0.0024
1.30	0.0256 ± 0.0020	0.0344 ± 0.0024
1.6	0.0253 ± 0.0016	0.0304 ± 0.0018
1.8	0.0230 ± 0.0014	0.0289 ± 0.0017
2.0	0.0229 ± 0.0012	0.0286 ± 0.0017
2.25	0.0218 ± 0.0015	0.0287 ± 0.0016
2.5	0.0223 ± 0.0013	0.0293 ± 0.0017
Boosted selection acceptance × efficiency		
g_{KK} mass [TeV]	e+jets	μ+jets
0.5	0.00037 ± 0.00009	0.00042 ± 0.00008
0.6	0.00107 ± 0.00023	0.00122 ± 0.00030
0.7	0.0030 ± 0.0008	0.0039 ± 0.0011
0.8	0.0085 ± 0.0016	0.0104 ± 0.0020
0.9	0.0143 ± 0.0016	0.0170 ± 0.0022
1.0	0.0180 ± 0.0017	0.0242 ± 0.0022
1.15	0.0233 ± 0.0014	0.0298 ± 0.0020
1.30	0.0259 ± 0.0015	0.348 ± 0.0021
1.6	0.0288 ± 0.0020	0.039 ± 0.004
1.8	0.0277 ± 0.0027	0.042 ± 0.005
2.0	0.026 ± 0.004	0.041 ± 0.007
2.25	0.0241 ± 0.0034	0.039 ± 0.007
2.5	0.0210 ± 0.0031	0.038 ± 0.008

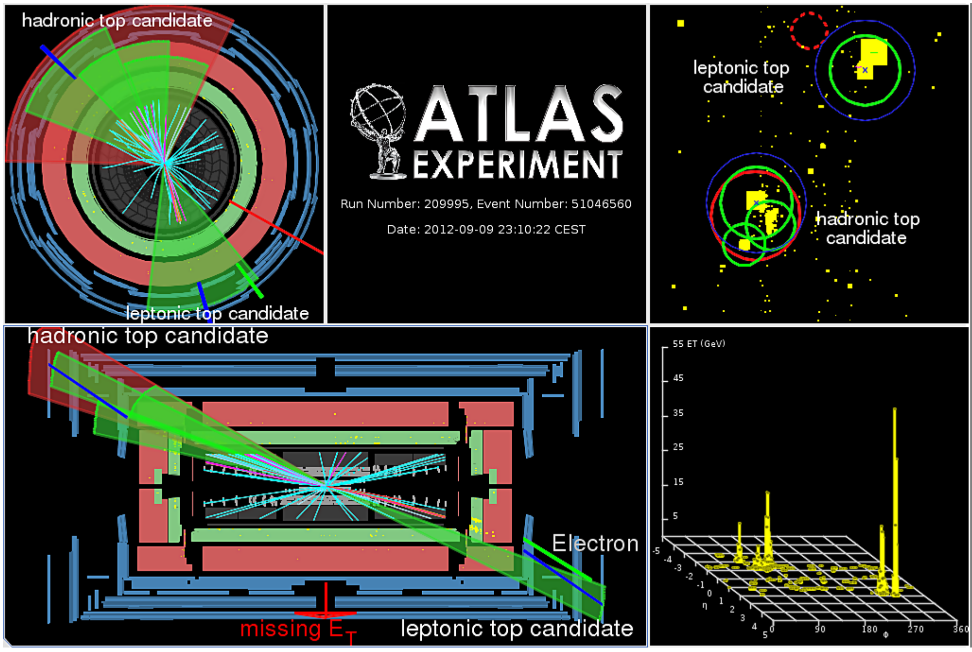

(a) e+jets event

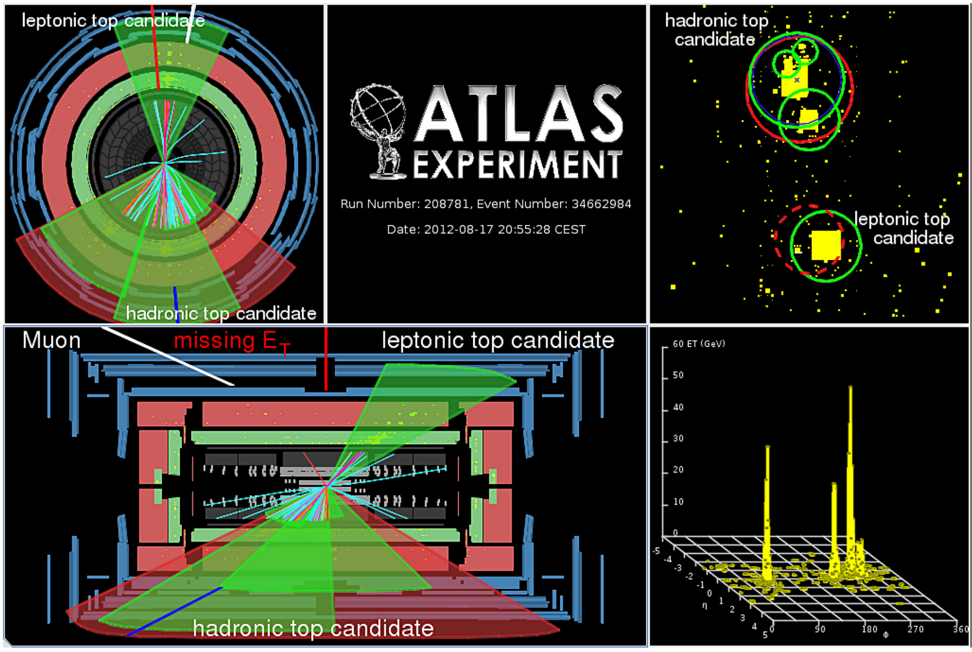

(b) μ+jets event

Figure 13: Event display for (a) $m_{t\bar{t}}^{\mathrm{reco}} = 2.6$ TeV e+jets (b) $m_{t\bar{t}}^{\mathrm{reco}} = 2.5$ TeV μ+jets $t\bar{t}$ candidate events. The upper left panel displays a transverse $(X - Y)$ view of detector and objects, while the lower left panel shows the longitudinal $(R - z)$ view. In these two views, jets are represented by circular sectors with their lengths proportional to the transverse energies. Green jets are reconstructed with R = 0.4, while red jets are reconstructed with R = 1. The b-tagged R = 0.4 jets are labelled with blue bars. An $\eta - \phi$ view of the same event is shown in the upper right panel, with the lego-plot of calorimeter energy in the lower right panel. In this plane, jets are represented by solid circles of the same color scheme, while the b-tagged ones are labelled by concentric blue circles. The red dashed circle represents the missing transverse momentum. The area of the circles are proportional to the transverse energy or momentum of the physics objects.